Pure and RE 3+ -Doped La7O6 (VO4) 3 (RE = Eu, Sm): Polymorphism Stability and Luminescence Properties of a New Oxyvanadate Matrix

María Alejandra Gómez Torres, Anna Kaczmarek, Gilles Gauthier, Marielle Huvé, Pascal Roussel, Valérie Dupray, Lina Yuan, Anastasiya Zadoya, Marie Colmont

Pure and RE^{3+}-doped $La_7O_6(VO_4)_3$ (RE= Eu,Sm) : polymorphism stability and luminescence properties of a new oxyvanadate matrix.

María Alejandra Gómez Torres,[1,2] Gilles H. Gauthier,[2] Anna M. Kaczmarek,[3, 4] Marielle Huvé,[1] Pascal Roussel,[1] Valérie Dupray,[5] Lina Yuan,[5] Anastasiya Zadoya[1], Marie Colmont[1*]

[1] Université Lille, CNRS, Centrale Lille, Université Artois, UMR 8181, Unité de Catalyse et Chimie du Solide, Lille, F-59000, France.

[2] Universidad Industrial de Santander, Grupo INTERFASE, Ciudad universitaria, Calle 9, Carrera 27, Bucaramanga, Santander, Colombia

[3] L^3 – Luminescent Lanthanide Lab, Department of Chemistry, Ghent University, Krijgslaan 281-S3, B-9000, Ghent, Belgium

[4] NanoSensing Group, Department of Chemistry, Ghent University, Krijgslaan 281-S3, B-9000, Ghent, Belgium

[5] Normandie Univ, UNIROUEN, SMS, 76000 Rouen, France

Abstract

Two polytypes of the new oxyvanadate matrix $La_7O_6(VO_4)_3$ were identified and deeply characterized. The crystal structure of the *α*-polytype was solved using a combination of precession electron diffraction and X-ray powder diffraction techniques. It crystallizes in a monoclinic unit cell with space group $P2_1$, a= 13.0148(3) Å, b= 19.1566(5) Å, c= 7.0764(17) Å and β= 99.87(1)°. Its structure is built upon $[La_7O_6]^{+9}$ polycationic units at the origin of a porous 3D networks evidencing rectangular channels filled by isolated (VO_4) tetrahedra. An *in situ* High Temperature XRD study highlights a number of complex phase transitions assorted with the existence of a *β*-polytype also refined in a monoclinic unit cell, space group $P2_1/n$, a= 13.0713(4) Å, b= 18.1835(6) Å, c= 7.1382(2) Å and β= 97.31(1)°. Thus, during the transitions, while the polycationic network is almost identical, the vanadate's geometry is largely modified. The use of Eu^{3+} and Sm^{3+} at different concentrations into the host lattice is possible using solid-state techniques. The photoluminescence (PL), PL excitation (PLE) spectra and luminescence decay times were recorded and discussed. The phosphors present an emission light being bright and reddish-orange after excitation under UV. This is mainly due to the V-O band and f-f transitions. Whatever the studied polytype, the final luminescence properties are retained during the heating/cooling process.

Introduction

The main idea dedicated to the study of inorganic compounds based on trivalent lanthanide ions (Ln^{3+}) is to find applications in many fields, ranging from optics, catalysis, electronics to biology.[1]–[7] The particular luminescence properties of Ln^{3+} cations result from transitions within the 4f structure levels, which are parity forbidden. As a consequence, the molar absorption coefficients are rather low whereas luminescent lifetimes are quite long. Different kind of phosphors were studied but, among them, vanadate-based compounds are of the most attractive. For example, $YVO_4:Eu^{3+}$ is a famous material used as red phosphor in the lamp industry because of its intense and pure red color related to the non-centrosymmetric site of Eu^{3+} cations. [8] In $GdVO_4:Eu^{3+}$, the energy efficient transfer occurring between vanadate and activators (Eu^{3+}) makes it an efficient material for displays.[9] In connection with what was already stated, $M_3(VO_4)_2$ (M= Sr and Ba) doped with rare earth is also an efficient phosphors used in lasers. All

these materials have in common a particular broadband emission in visible light assigned to VO_4^{3-} groups.[10] These tetrahedra are hosting charge transfer phenomena leading to a high emitting intensity, which depends on the degree of distortion of each tetrahedron. In order to obtain even better performance, the search for luminescent materials is devoted to (1) the modifications of already evidenced host matrix and (2) the search for innovative phosphors. Studies performed on $NaALa(VO_4)_2$, (A= Ca, Sr or Ba), [11] $LiSrVO_4$, [12] $CsK_2Gd(VO_4)_2$ [13] or again YVO_4 have been described.[8] All these phosphors exhibit bright red emissions under UV excitation by Eu^{3+} doping, the subsequent quantum yield being directly related to the intense absorption of UV light stemming from the vanadate group and the strong energy transfer from VO_4 tetrahedra to Eu^{3+} cations. As a consequence, interesting host lattices for such application can be found in the combination of vanadate groups with non-active lanthanum or yttrium rare-earth, considering that most of the luminescent trivalent lanthanide (Ln^{3+}) cations can generally substitute for La or Y. Recently, our group fully characterized the new $KLa_5O_5(VO_4)_2$ in terms of crystal structure and optical properties, its color changing from blue to orange/red by Eu^{3+} doping.[14] Following the discovery of this new compound, potassium was replaced by other alkali metals: Li, Na, Rb and finally Cs. While the synthesis was successful with Li, Na and Rb, it results in an unknown phase identified during the preparation of $CsLa_5O_5(VO_4)_2$ powder sample. The final new phase, purpose of the present manuscript, of composition $La_7O_6(VO_4)_3$, was obtained as pure powder phase. A complete description of the structure of this new material, not only at room temperature, but also as a function of temperature, is described in the present paper, as well as the optical properties resulting from the substitution of Eu^{3+} and Sm^{3+} for La^{3+}.

2. Experimental section

2.1 Synthesis. In a first attempt, our goal was to synthesize a sample of composition $CsLa_5O_5(VO_4)_2$ homologous to $KLa_5O_5(VO_4)_2$. [14,21] It was prepared from a stoichiometric amount of Cs_2CO_3, La_2O_3 and V_2O_5 (preliminary heated respectively at 1000°C and 500°C during 1h to remove residual water or carbonate molecules). The mixture was ground in an agate mortar, placed in an alumina crucible, and successively heated at 500°C and 900°C for 12h, then finally at 1200°C during 24 h. After heating, all samples were quenched. An electron microscopic

study allowed deduction of a preliminary structural model (see below) and a good estimation of the chemical formula (i.e. the absence of cesium, see after) ; the synthesis of pure polycrystalline $La_7O_6(VO_4)_3$ compounds was performed in the same conditions.

Polycrystalline powder samples of the lanthanide doped series $La_{7-x}Ln_xO_6(VO_4)_3$ (Ln= Eu or Sm; x= 0.14, 0.35 and 0.7) were prepared by the same method, using $Eu(NO_3)_3.5H_2O$ and Sm_2O_3 as europium and samarium source, respectively. All compositions were obtained as white powders.

2.2 Structure refinement from Electron Microscopy.

The grain shape and size of the $La_7O_6(VO_4)_3$ doped 5% Sm^{3+} and Eu^{3+} powder were investigated using a scanning electron microscope (Hitachi S-3400N apparatus).

TEM (Transmission Electron Microscopy) and EDX (energy-dispersive X-Ray spectroscopy) investigation were done using a FEI Tecnai G2.20 microscope. Electron diffraction patterns (EDP) were registered with the Nanomegas Spinningstar system and a 14 bits dynamic range ORIUS 832 Gatan CCD camera. The conditions of 3D electron diffraction tomography study are gathered in Table 1.

Table 1: PEDT experimental details

Data collection	
TEM acceleration voltage, wavelength	200kV, 0.00251 Å
Sample holder	Holey Carbon grid - copper
Precession angle	1.2°
Number of patterns	118
Tilt angles	From -57° to +60° (step every 1°)
Practical details	
Software used for the processing of electron diffraction tomography data	PETS [15], [16]
Software used for the structure-solution	Superflip [17]
Software used for the structure-refinement	Jana2006 [18], kinematical approach

2.3 Powder X-Ray Diffraction analysis. Data were collected in a first step, at room temperature (RT), using a Rigaku SmartLab X-ray diffractometer working with a 9kW rotated anode X-ray generator, delivering Cu $K\alpha_{1,2}$ radiations, in the $2\theta=5°$ to $2\theta=120°$ range, with 0.02° step and a counting time optimized to ensure a good counting statistic. The Rietveld refinement was

performed using the Jana2006 software [18]. In a second step, and to measure patterns in temperature, a diffractometer D8 ADVANCE (Bruker-AXS) was used. It is working in Bragg Brentano geometry and equipped with a 1D LynxEye detector. The patterns were measured every 25 °C from RT to 850 °C (heating rate of 10 °C min^{-1}), in air. The sample holder was placed inside an Anton-Paar XRK900 furnace.

2.4. XRF analysis. A Rigaku NEX CG Energy Dispersive X-ray Fluorescence (EDXRF) spectrometer was employed for the precise determination of the Ln^{3+} concentrations in the samples. Low energy "soft" X-rays (1-50 keV) arise from an x-ray tube. The concentration of the Ln^{3+} elements in each sample was calculated using the NEX CG software.

2.5 Luminescence properties. The luminescence was measured on solid powdered samples. The powders were deposited between quartz plates. Luminescence study was done on an Edinburgh Instruments FLSP920 UV-vis-NIR spectrometer setup. A xenon lamp (450W) was used as the stable state excitation source. A 60W pulsed Xe lamp was employed to record the luminescence decay times (lamp was operating at a frequency of 100 Hz). The emission signals in the near UV to visible range were detected by using a Hamamatsu R928P photomultiplier tube. All measurements were carried out at RT. The detector response was systematically subtracted to all emission spectra. The decay times were registered after excitation into the highest V-O charge transfer band and monitored at the maximum emission peak. The decay curves could be satisfactorily fitted with a single exponential or a biexponential function (Eq. 1 and 2, respectively).

$$I = A \exp\left(-\frac{t}{\tau}\right) \qquad \text{Eq.1}$$

$$I = A_1 \exp\left(-\frac{t}{\tau_1}\right) + A_2 \exp\left(-\frac{t}{\tau_2}\right) \qquad \text{Eq. 2}$$

where I is the luminescence intensity and A, A_1 and A_2 are constants, t is time and τ, τ_1 and τ_2 are the luminescence lifetimes. Quantum yields (QYs) were measured with an

integrating sphere (provided by Edinburgh Instruments, covered in BENFLEC) and computed with equation 3:

$$\eta = \frac{\int L_{emission}}{\int E_{blank} - \int E_{sample}} \qquad Eq.3$$

where $L_{emission}$, E_{blank} and E_{sample} are respectively the integrated zone under the emission spectrum, under the "excitation" band of the blank, and under the excitation band of the sample.

2.6 Temperature-Resolved Second Harmonic Generation (TR-SHG).

The TR-SHG method is described in detail in references. [19], [20] Herein, the sample (few mg of powder in an amorphous SiO_2 crucible) was inserted in a computer-controlled heating-cooling stage and cooled at 10 K/min between 500 and 20°C. The SH signal generated by the sample upon laser irradiation was recorded every 50 °C, during 3s (30 laser pulses). The number and duration of the measurements were chosen in order to avoid degradation of the sample under the beam and to ensure the best stability of the laser energy. The SH signal versus temperature plot was obtained by normalizing the SH raw values with the maximum SH intensity recorded. Error on the SH values (principally due to energy variations of the laser beam) was estimated to ca. 3%.

3. Results and discussion

3.1 Evidence of the new phase. After reporting on the preparation of the $KLa_5O_5(VO_4)_2$ new phase and related Li, Na, and Rb ones [21], we decided to embark on the synthesis and study of the luminescent properties of the Cs-analogue series. However, the as-obtained X-ray diffraction pattern was different from those of the former compounds, evidencing the presence of a predominant phase, hereinafter referred to as α-phase (see below), that has no similarities in the ICDD database. The XRDP was successfully indexed using DICVOL software [22] in a monoclinic unit cell with parameters *a*= 13.03 Å, *b*= 19.3 Å, *c*= 7.09 Å and *β*= 99.9°. A

complementary EDS analysis confirmed the presence of lanthanum and vanadium in a La:V=24:9 ratio (average over 10 different crystals), excluding the presence of cesium. Using such ratio (*i.e.* without cesium), a new preparation led to the same diffraction pattern, *i.e.* the same phase. Our efforts to solve the structure using *ab initio* technique were unsuccessful and, in front of the impossibility to grow single crystals of the same composition, we tried to solve the structure using PEDT.

3.2 Electron Diffraction Study. The 3D reciprocal space reconstruction confirms a monoclinic unit cell with parameters for the α-phase closed to: a≈13 b≈19 c≈7 Å and β≈ 100° and an extinction rule corresponding to *0k0* reflections with *k=2n+1*. The basic patterns shown in Figure 1 exhibit no extra conditions. The comparison between the ZOLZ (Zero Order Laue Zone) and the FOLZ (First Order Laue Zone) leads to an extinction symbol $P12_11$. The *0k0 k=2n+1* spots also viewable in Figure 1 are systematically generated by double diffraction and disappear by rotation.

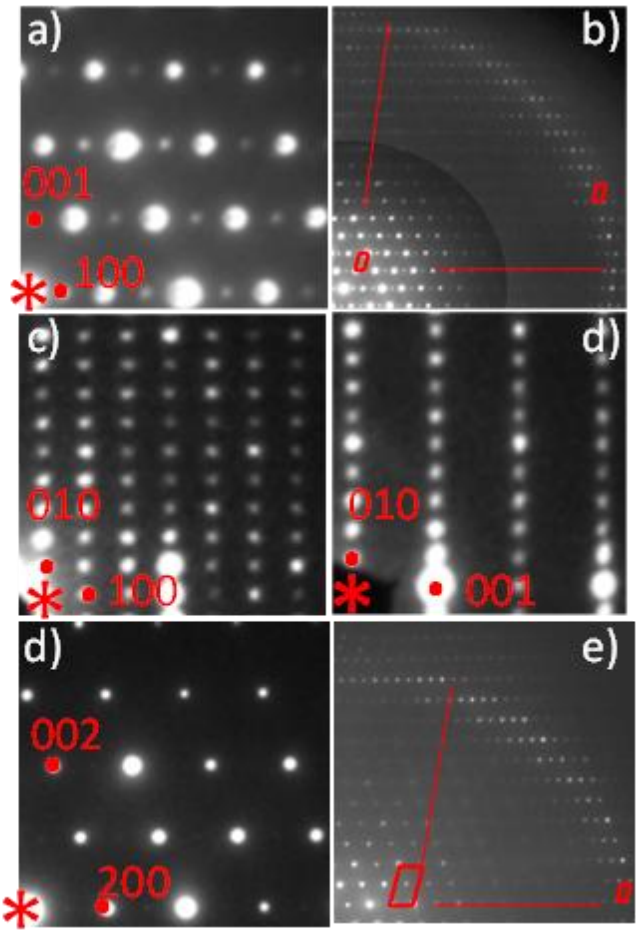

Figure 1: α-$La_7O_6(VO_4)_3$: a) [010] zero order Laue zone ; b) Comparison of [010] Zero and First order Laue zone showing no shift or difference of periodicity leading to a P1-1 extinction symbol (- means no glide plan) c) [001] and d) [100] oriented zone axis pattern (ZAP). β-$La_7O_6(VO_4)_3$: a) [010] zero order Laue zone b) Comparison of [010] zero and first order Laue zone showing no shift but a difference of periodicity leading to a P1n1 extinction symbol

3.3 Structure Model deduced from PEDT and Kinematical Refinement.

PEDT (Precession electron diffraction tomography) data were collected on a nanocrystal and applying the process of Kolb *et al.* [23] and previously applied in our lab in ref [21]. The unit cell parameters: a= 7.0054(9)Å, b= 18.938(6)Å, c= 12.841(2)Å, α= 90.04(2), β= 99.85(1), γ= 89.95(2)° were deduced from the position of electron diffraction spots using Jana2006[18]. After indexing step, the integration of intensities by PETS using the kinematical mode, resulted in 10936 pseudo-kinematical intensities that were afterward imported in Jana2006. As mentioned in the preliminary SAED study, space group $P2_1$ was chosen for the structure solution, also

confirmed using the charge-flipping method implemented in Superflip [17]. The deduced formula is $La_7V_3O_{18}$, confirming the EDX results. Attempts to use dynamical refinements, leading in general to a more accurate model (see the discussion in [21]) were systematically unsuccessful, probably due to the poor quality of the samples; however, the sample quality was good enough for the as-presented pseudo-kinematical approach. We thus decided to refine our model using the well-known X-ray powder Rietveld approach, with the PEDT solution as starting model.

3.4 Rietveld Analysis. At this step, the chemical composition obtained from the pseudo-kinematical model was used to prepare a pure powder sample, according to the experimental details given in section 2. A good-statistic powder XRD pattern was then recorded to perform an accurateRietveld structure refinement of α-$La_7O_6(VO_4)_3$. The measurements were done under experimental conditions detailed in Table 2. Prior to Rietveld refinement, a Second Harmonic Generation (SHG) study was performed at ambient temperature to confirm the non-centrosymmetric space group. An SHG signal of 18% was obtained, compared to quartz, in agreement with a non-centrosymmetric space group. It is noteworthy that the sample rapidly degrades under the laser beam. Because the ED analysis highlighted the $P2_1$ space group in agreement with the SHG study, the latter symmetry was selected for the refinement (unit cell a= 13.0148(3) Å, b= 19.1566(5) Å, c= 7.0764(2) Å and β= 99.87(1)°). The structural model deduced from kinematic PEDT data gave the initial positions of all atoms. The refinement swiftly converged with good values of atomic displacement parameters (ADP). The (VO_4) tetrahedra are regular and ordered. The experimental and calculated patterns are shown in Figure S1 indicating that the structure determined from PEDT data perfectly fits the experimental powder pattern. The atomic coordinates and ADP are gathered in Table S1. The structural data for α-$La_7O_6(VO_4)_3$ phase were deposited at the Cambridge Structure Database (No. CSD-1971852).

Table 2: Refined structural data for α and β-$La_7O_6(VO_4)_3$.

General data		
	α -$La_7O_6(VO_4)_3$	**β-$La_7O_6(VO_4)_3$**
Source	Laboratory X-Ray	
Formula Weight (g/mol)	1414.76	1417.16
Temperature (K)	293	
Wavelength	Cu Kα	
Theta range (°)	5-120	
Crystal system	Monoclinic	

Space group	$P2_1$ (n°4)	$P2_1/n$ (n°14)
Z	2	4
Cell parameters		
a(Å)	13.0148(3)	13.0713(4)
b(Å)	19.1566(5)	18.1835(6)
c(Å)	7.0764(17)	7.1382)(2)
β(°)	99.87(1)	97.31(1)
V(Å^3)	1738.16(8)	1682.8(2)
Statistical parameters for Rietveld refinement		
$\mathbf{R_P}$	3.41	3.83
$\mathbf{\omega R_P}$	4.80	5.45
GOF	2.79	3.29
$\mathbf{R_{all}}$	8.69	2.43
$\mathbf{R_{obs}}$	8.38	2.91
$\mathbf{\omega R_{obs}}$	8.71	4.28

3.5 Crystal Structure Description of α-$La_7O_6(VO_4)_3$. As already noticed for other lanthanide-based oxides, the new phase is properly described using the antiphase approach involving association of tetrahedra centered on oxygen and surrounded by lanthanum. These (OLa_4) units are sharing edges and corners to set up $[La_7O_6]^{+9}$ polycationic units at the origin of a porous 3D networks. The structure is presented on Figure 2a, evidencing rectangular channels filled by isolated (VO_4) tetrahedra. This original structure is interesting because it is the first one, in the binary systems La_2O_3-V_2O_5, to be reported as oxo-centered. The [001] and [100] HAADF images are shown Figure 3. The lanthanum atoms take place in the white zones whereas vanadium stand in the darker regions. These images confirm the perfect stacking of this structure, which reminds the reported $Ln_7O_6(BO_3)(PO_4)_2$ series (Ln= Gd and Pr) [24]. In the latter, a borate group substitutes a phosphate tetrahedron leading to a slightly different chemical formula. The flexibility of the channel induced by the possibility to replace a borate by a vanadate group encouraged us to check the thermal stability of this new phase. Nevertheless, the $Ln_7O_6(BO_3)(PO_4)_2$ series are refined in the centrosymmetric space group $P2_1/n$. Here, our studies confirm the non-centrosymmetric behavior of α-$La_7O_6(VO_4)_3$ phase with S.G. $P2_1$. It is noteworthy that several oxo-centered units hosting isolated vanadate groups show thermal structure transition due to the reorganization with temperature of the (VO_4) tetrahedra around the polycationic walls. The orientation change of the vanadate unit, at the origin of the symmetry

lowering with temperature, involves also a modification of the physical properties such as SHG in $BiCa_2(As,V)O_6$ or $BiCd_2VO_6$ [25], [26]. To check the existence of potential phase transitions (that would be essential for thermal sensor application, for instance), an *in situ* HTXRD study was performed under air.

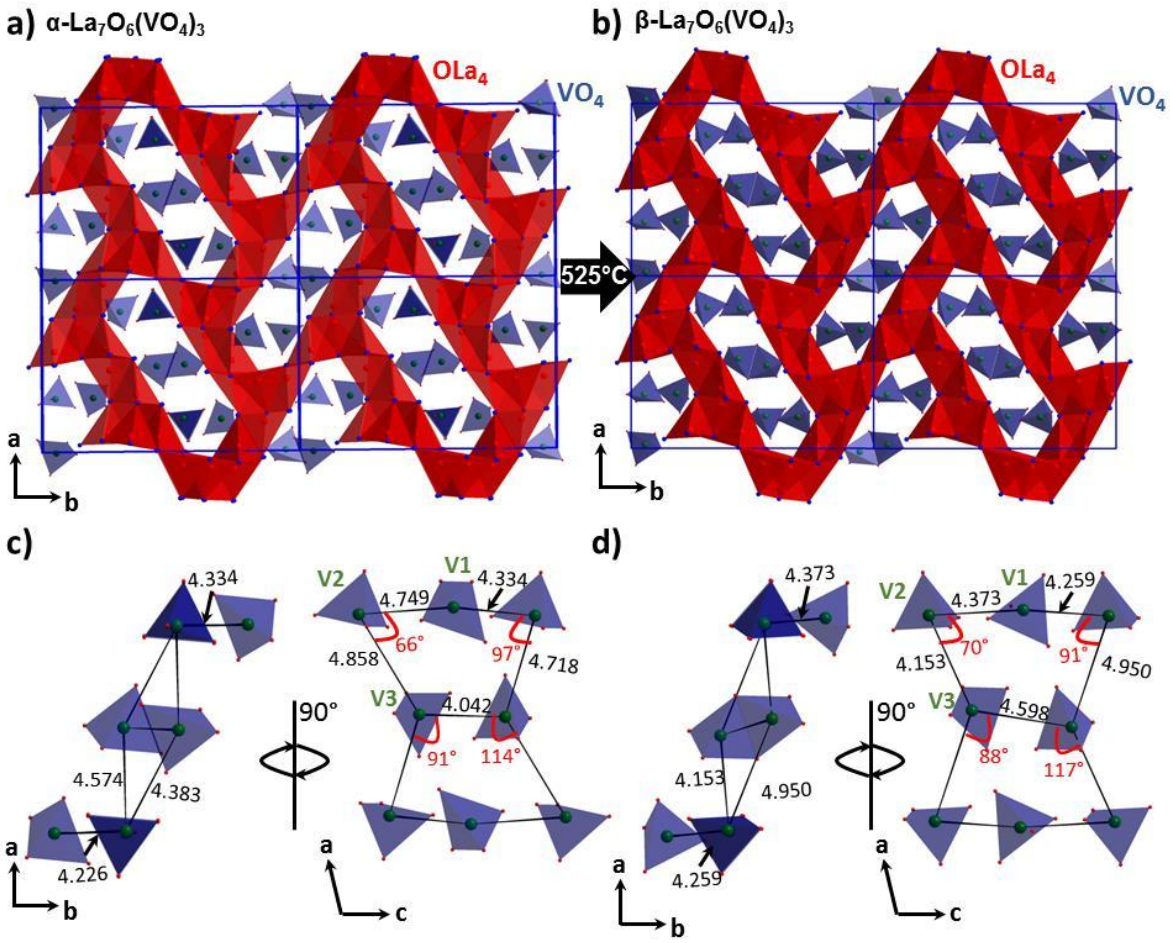

Figure 2: Crystal structure of a) α-$La_7O_6(VO_4)_3$ and b) β-$La_7O_6(VO_4)_3$ showing the $[La_7O_6]^{9+}$ polycationic backbone in red. 1D tunnels are evidenced, which host isolated (VO_4) tetrahedra. Main V-V distances (in Å) and V-V-V angles (in degrees) inside tunnels for c) α-$La_7O_6(VO_4)_3$ and d) β- $La_7O_6(VO_4)_3$.

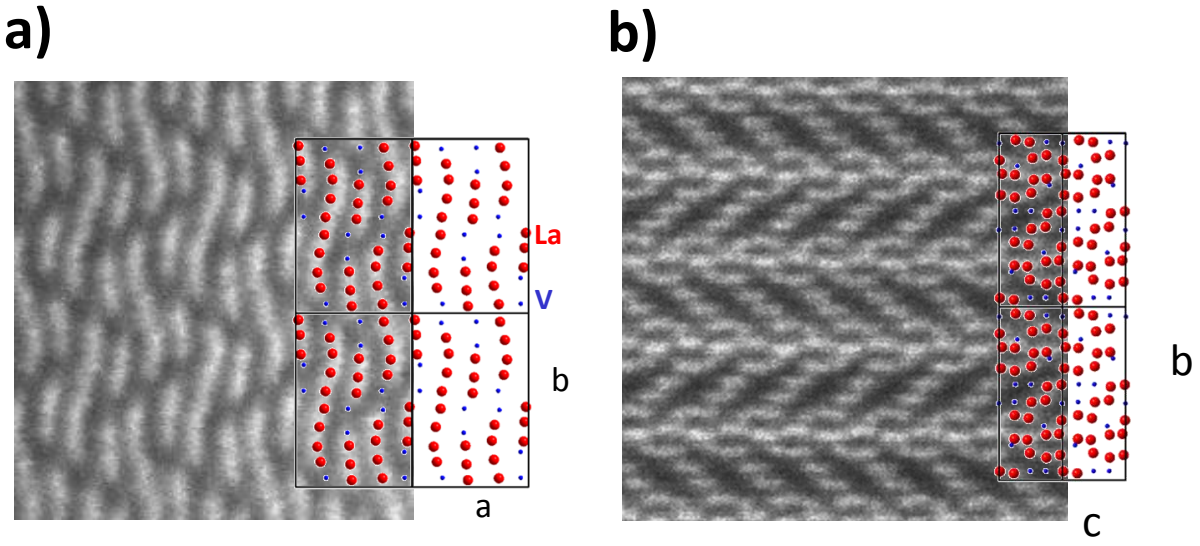

Figure 3: a) [001] and b) [100] HAADF images of α-$La_7O_6(VO_4)_3$ and structure projection of heavy atoms.

3.6 Temperature X-Ray Study of α-$La_7O_6(VO_4)_3$. Figure 4 shows a 2D representation of the evolution with temperature of diffractograms measured for $La_7O_6(VO_4)_3$. Even if the evolution appears to be complex, a careful analysis of the diagrams assorted with systematical refinement of the unit cell parameters point out the existence of a second polytype hereafter labelled β, the α phase being the RT stable polytype. The β-phase is also monoclinic, with refined lattice parameters a= 13.0713(4) Å, b= 18.1835(5) Å, c= 7.1382(2) Å and β= 97.31(1)°. Alongside the HTXRD study, we performed a SHG vs temperature study, which showed the presence of a transition from a non-centrosymmetric to a centrosymmetric structure above 450° (Figure S2). The β-structure was thus refined in $P2_1/n$ as the crystal structures reported for the $Ln_7O_6(BO_3)(PO_4)_2$ series and according to the extinction symbol P1n1 deduced from the ED observation (Figure 1). The structural data for β-$La_7O_6(VO_4)_3$ phase was deposited at the Cambridge Structure Database (No. CSD-1971853).

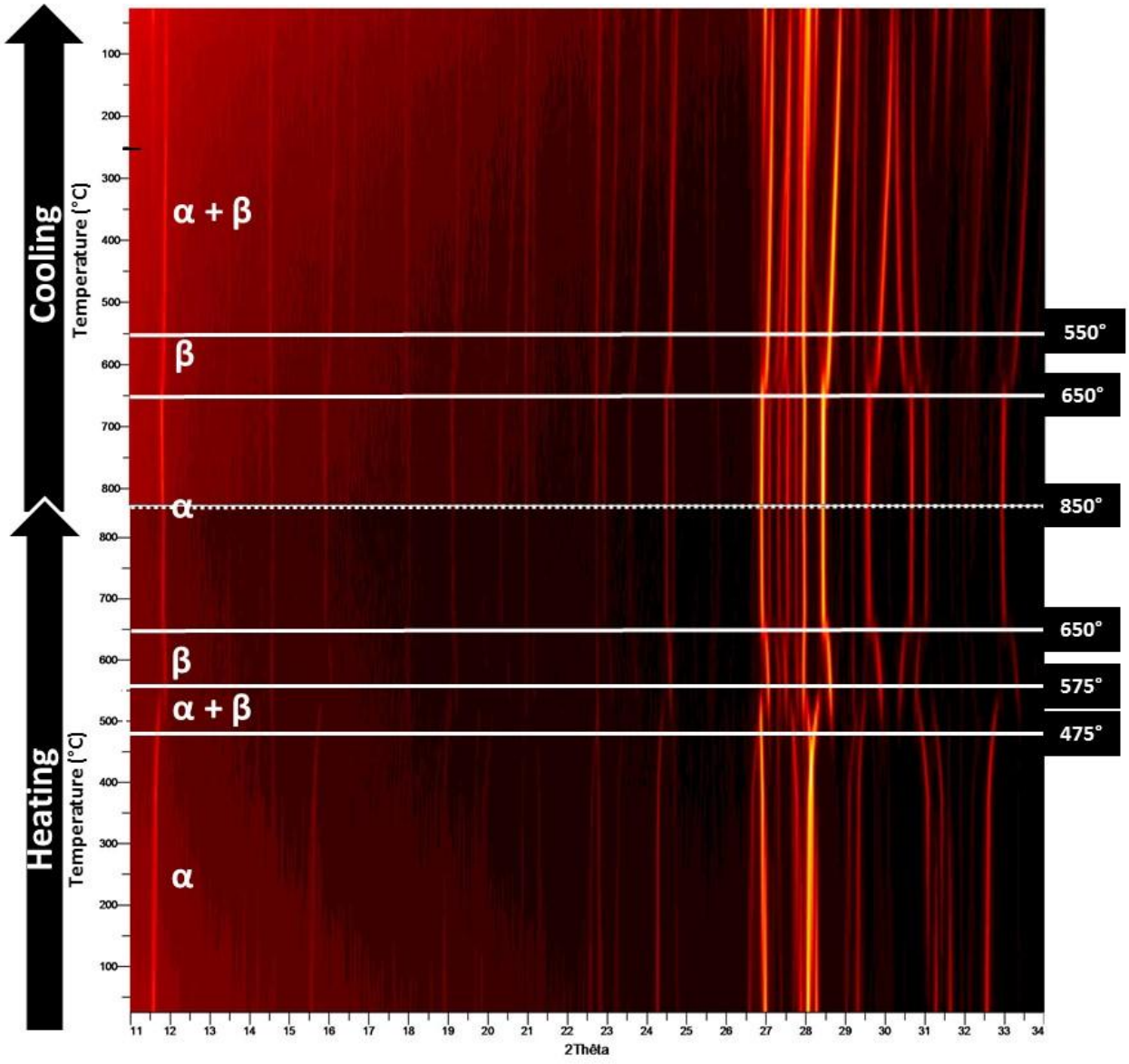

Figure 4: HT-XRDP of α-$La_7O_6(VO_4)_3$ in air from 50 to 850°C showing a complex phase transition scheme: α → α +β → β → α on heating, and α → β → α +β on cooling back to RT.

Concerning the HTXRD analysis, a first phase transition corresponding to α→ α +β is evidenced on heating around T=475 °C in good agreement with the TR-SHG study (see figure S2. Supplementary Information). It is followed by another structure change corresponding to α +β → β at T=575 °C, before finally come back to α structure around 650 °C. On cooling, two different phenomena are evidenced: the first one observed around T=650°C and corresponding to the reversible phase transition α → β and a second one at 550°C that corresponds to the phase demixtion β → α+β. The evolution of the unit cell parameters clearly highlights these structural

transitions. The evolution of *b* lattice parameter highlights clearly the evolution of the cell along with temperature, as detailed in Figure 5. It is noteworthy that, although the evolution of the powder diffraction pattern is clear (Figure 4), only "minor" structural changes occur: while the (VO_4) tetrahedra are rotating, the main polycationic $[La_7O_6]^{9+}$ backbone remains almost unchanged. A second-order phase transition is foreseen as there is no evidence of anomaly on DTA (Differential Thermal Analysis) when the α-polytype is transformed into β-$La_7O_6(VO_4)_3$. Such phenomenon was already evidenced on oxo-centered structures including vanadate groups, for example in $PbBiVO_5$ and Pb_2BiVO_6. [27], [28] In the present case, the rotation of vanadate tetrahedra is illustrated in Figure 2.

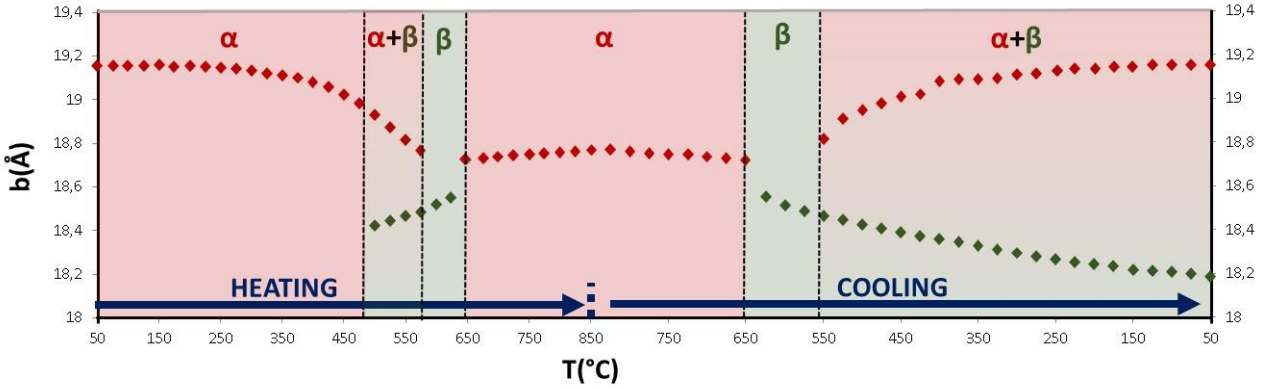

Figure 5: Evolution with temperature of *b* lattice parameter highlighting the main structural transitions during heating and cooling.

3.7 Luminescence study of Eu and Sm-doped $La_7O_6(VO_4)_3$. In order to study their optical properties, $La_{7-x}Ln_xO_6(VO_4)_3$ compounds with Ln= Eu, Sm and *x*= 0.14, 0.35 and 0.7 (corresponding to 2, 5 and 10 mol% of the La site, respectively) have been synthesized and fully characterized. LeBail-type whole pattern matching using XRD data for the above-mentioned doped samples are shown Figure 6. For both dopants and at low concentration, all peaks go to the unit cell and space group corresponding to the α-$La_7O_6(VO_4)_3$ polytype. From 10% and 5% doping rates, for Sm^{3+} and Eu^{3+}, respectively, a second phase is observed. After careful analysis, the latter corresponds to β- polytype of $La_7O_6(VO_4)_3$. In fact, the smaller effective ionic radii of Sm^{3+} (r= 1.079Å, CN=8) and Eu^{3+} (r=1.066Å, CN=8)[29] in comparison to La^{3+} (r= 1.16Å, CN=8)) affect the chemical pressure and induce the presence of the second phase. Here the reduction of the ionic radii

goes with a smaller unit cell volume that stabilize preferentially the β-polytype. Refined unitcell parameters are gathered in Table 3. The real doping percentages were determined by XRF and are shown in Table S2.

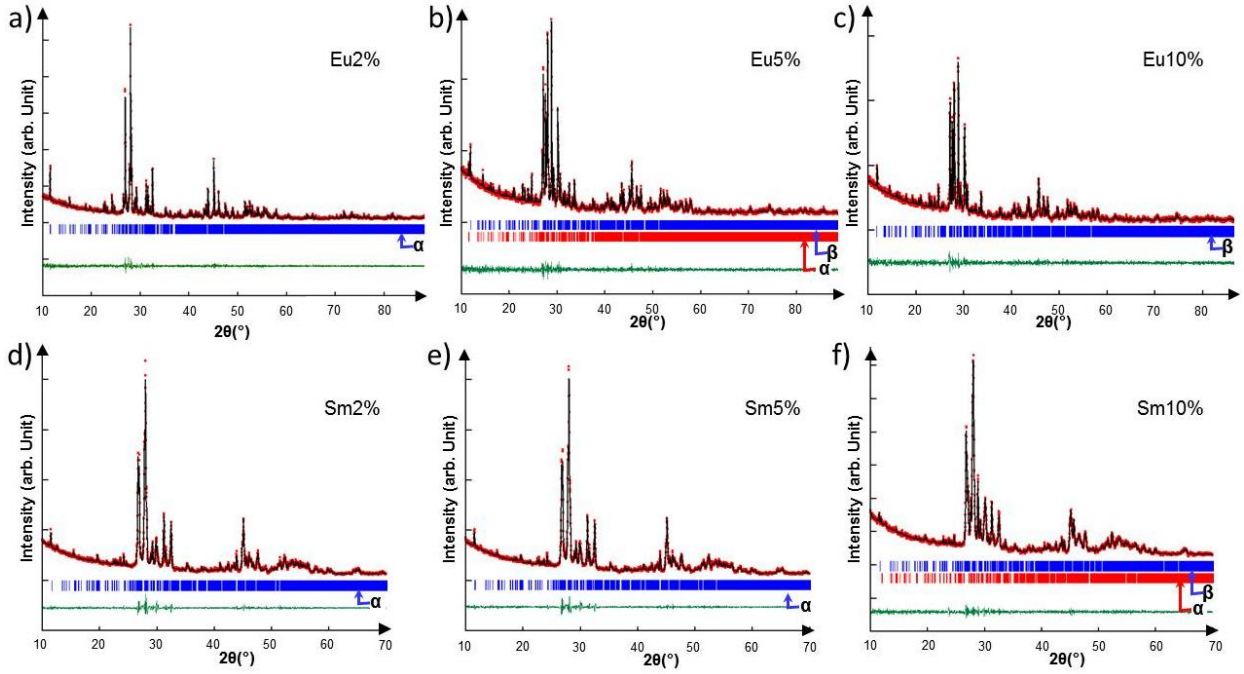

Figure 6: Pattern matching refinement plot of $La_{7-x}Ln_xO_6(VO_4)_3$ with a) Ln= Eu and x= 0.14, b) Ln= Eu and x= 0.35, c) Ln= Eu and x= 0.7, d) Ln= Sm and x= 0.14, e) Ln= Sm and x= 0.35 and f) Ln= Sm and x= 0.7. The observed X-ray diffraction intensity appears in red and the calculated curve in black. The bottom curve in green is the difference of patterns, yobs – ycalc, and the small red and blue bars show the angular positions of the Bragg reflections of the α- and β-polytypes.

Table 3: Refined unit cell parameters of doped $La_{7-x}Ln_xO_6(VO_4)_3$ (Ln= Eu^{3+} and Sm^{3+}) with x= 0.14, 0.35 and 0.7.

$La_{7-x}Ln_xO_6(VO_4)_3$			a(Å)	b(Å)	c(Å)	β(°)	V(Å^3)
Undoped	**α-phase**		13.0148(3)	19.1566(5)	7.0764(17)	99.87(1)	1738.16(8)
Undoped	**β-phase**		13.0713(4)	18.1835(6)	7.1382(2)	97.31(1)	1682.8(2)
Sm^{3+}	**x=0.14**	**α-**	13.0202(13)	19.1457(18)	7.0899(7)	100.11(1)	1739.95(48)
		β-	-	-	-	-	-
	x=0.35	**α-**	13.0141(8)	19.1302(11)	7.0863(4)	100.11(1)	1736.83(26)
		β-	-	-	-	-	-

	x=0.7	**α-**	13.0184(8)	19.1300(14)	7.0867(5)	100.29(1)	1736.49(26)
		β-	13.0534(9)	18.1993(12)	7.1215(5)	97.38(1)	1676.88(26)
Eu^{3+}	**x=0.14**	**α-**	13.0063(3)	19.1342(4)	7.0746(2)	99.86(1)	1734.61(9)
		β-					
	x=0.35	**α-**	13.0077(6)	19.1302(8)	7.0729(4)	99.88(1)	1733.95(17)
		β-	13.0535(9)	18.1775(14)	7.1316(5)	97.30(1)	1678.51(19)
	x=0.7	**α-**	-	-	-	-	-
		β-	13.0331(6)	18.1497(8)	7.1163(4)	97.34(1)	1669.53(17)

Obviously, the morphology and size of powder impact the luminescence properties of a sample. Figure S3 shows a SEM image of $La_7O_6(VO_4)_3$ doped 5% Eu^{3+} and Sm^{3+}. This image shows a clear aggregation of non-regular and thin platelet-like crystals. Their size is variegated and mainly below micrometer.

The photoluminescence properties of the 6 samples and the pristine material were studied. Combined excitation-emission spectrum of $La_7O_6(VO_4)_3$ is shown figure S4. The spiky peaks in the emission spectrum is most probably related to the Xenon lamp.

In all, concerning all the Eu^{3+} doped samples, the excitation spectrum includes a broad V-O band in the 250 – 350 nm range with a maximum at 320 nm and few sharp peaks assigned to the characteristic Eu^{3+} transitions. Figure 7 shows the RT combined excitation and emission spectrum of 2%Eu:$La_7O_6(VO_4)_3$. All three samples were excited at 320 nm (into the V-O band) and at 464 nm (in the f-f transition). When exciting into the f-f transitions (at 464 nm), a stronger emission intensity is observed. In the emission spectra obtained when exciting at both wavelengths, the typical $^5D_0 \rightarrow ^7F_{0\text{-}4}$ transitions are detected (at 578 nm, 599 nm, 615 nm, 655 nm and 706 nm, respectively). The exact assignment of all bands in the spectra is given in Table S3. The excitation and emission spectra of 5%Eu:$La_7O_6(VO_4)_3$ and 10%Eu:$La_7O_6(VO_4)_3$ samples are also presented in SI (Figures S5 and S6). The spectra look almost identical, with some variations in the intensity of the V-O charge-transfer band in the excitation spectrum. The intensity of the emission spectra of the three samples are compared in Figure 8. As can be clearly evidenced, the highest intensity is observed for the 10%Eu:$La_7O_6(VO_4)_3$ material. An in-

depth analysis of the $^5D_0 \rightarrow {}^7F_1$ peak splitting in these samples suggests multiple Eu^{3+} sites in the materials. This is in agreement with the crystallographic data. Furthermore, the luminescence decay times for these samples were recorded when exciting both into the V-O band as well as into the $^5D_2 \leftarrow {}^7F_0$ transition band. The decay profiles for the 2%. 5% and 10% samples are given in SI (Figures S7 to S9). In all cases, the decay profiles could only be well fitted using a biexponential fit, suggesting again more than one Eu^{3+} center. The calculated decay time values are summarized in Table 4. Interestingly, the decay time recorded when exciting into the V-O band is always longer for all three samples when compared to an excitation at 464 nm. The longest decay times were recorded for the of $Eu:La_7O_6(VO_4)_3$ sample (742 µs upon 320 nm excitation and 610 µs upon 464 nm excitation). We observe a decrease in the decay time at higher concentrations, which is due to concentration quenching processes. The QYs of the samples were recorded (both overall and intrinsic). For 2%Eu sample the overall QY = 0.14%, intrinsic QY = 1.26%. For 5%Eu sample the overall QY = 0.44%, intrinsic QY = 1.78%. For 10%Eu sample the overall QY = 0.65%, intrinsic QY = 2.28%. Although these values are low there is clearly visible a rise in the QYs values upon concentration increase.

Table 4: Luminescence decay times of $Eu:La_7O_6(VO_4)_3$ samples

Sample	τ (µs) exc 320nm	τ (µs) exc 464nm
$2\%Eu:La_7O_6(VO_4)_3$	742	610
$5\%Eu:La_7O_6(VO_4)_3$	707	538
$10\%Eu:La_7O_6(VO_4)_3$	695	544

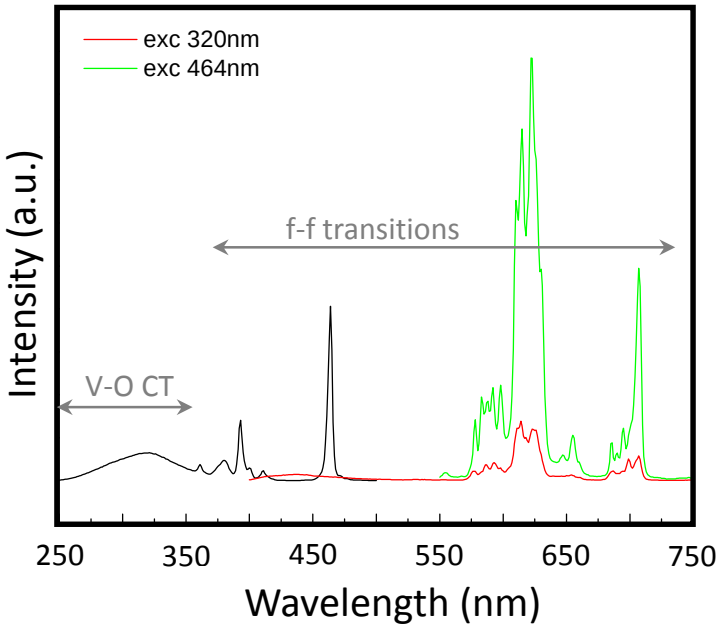

Figure 7: Room-temperature combined excitation-emission spectrum of 2%Eu:$La_7O_6(VO_4)_3$.

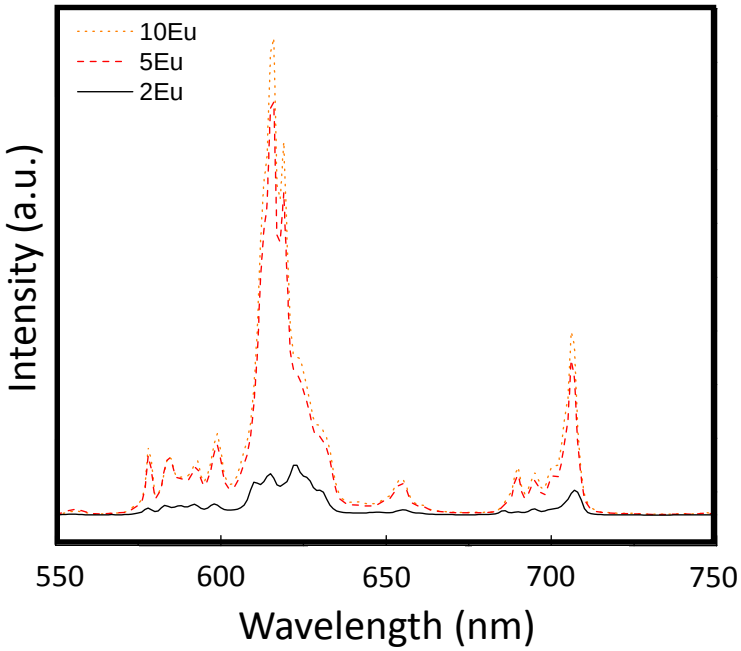

Figure 8: Emission spectra of 2%Eu:$La_7O_6(VO_4)_3$, 5%Eu:$La_7O_6(VO_4)_3$, and 10%Eu:$La_7O_6(VO_4)_3$ (excited at 464 nm).

In addition, we examined the case of Sm:$La_7O_6(VO_4)_3$ samples, also prepared at 2%, 5% and 10% doping levels. Figure 9 presents the combined excitation-emission spectra of sample 2%Sm:$La_7O_6(VO_4)_3$, while the spectra of the two other samples are given in SI (Figures S10 and S11). In these samples, the excitation spectrum corresponds also of a broad V-O charge transfer band between 250 and 350 nm, with a maximum at 322 nm, as well as a series of sharp f-f transition peaks, which can be assigned to the characteristic Sm^{3+} transitions. The emission spectra were registered when exciting at 322 nm into the V-O band as well as when exciting at 404 nm into an f-f transition. In both cases, the characteristic Sm^{3+} emission bands are observed: $^5G_{5/2} \rightarrow {}^6H_{5/2}$, $^5G_{5/2} \rightarrow {}^6H_{7/2}$, $^5G_{5/2} \rightarrow {}^6H_{9/2}$, $^5G_{5/2} \rightarrow {}^6H_{11/2}$. The assignment of the peaks to appropriate transitions is given in Table S3. The emission intensity of the 2%, 5% and 10% Sm:$La_7O_6(VO_4)_3$ samples has been compared in Figure 10. The strongest intensity is measured for 5%Sm:$La_7O_6(VO_4)_3$ material, but it is very similar to the case of 2%Sm:$La_7O_6(VO_4)_3$. The emission of 10%Sm:$La_7O_6(VO_4)_3$ compound shows weakest intensity, which is in agreement with previously reported results.[30] For the Eu^{3+} samples, concentration quenching was not observed even at 10% doping, whereas in the case of Sm^{3+}, concentration quenching is observed above 5% doping, with a significant drop in intensity for the 10% sample. The low concentration quenching of the Sm^{3+} ions in the samples (compared with Eu^{3+} ions) may be due to cross-relaxation activity for samarium cations.[31] This process is detailed as ($^4G_{5/2}$) + Sm^{3+} ($^6H_{5/2}$) → 2Sm^{3+} ($^6F_{9/2}$). Concerning the Eu^{3+} centers, no such cross-relaxation effect exists (All things considered, the cross-relaxation will reduce the quenching concentration of the activator ion). For the 10%Sm:$La_7O_6(VO_4)_3$ sample, a broad band in the region 400–540 nm is additionally observed in the emission spectrum (see Figure S12). This is not observed for the other two concentrations. This most likely originates from some energy back transfer to the V-O band.[32] It is observed both when exciting at 322 nm as well as 404 nm. Our materials show a much faster concentration quenching compared to for example the work of Zhu et al. where in a Sm:$La_7O_6(BO_3)(PO_4)_2$ matrix 7%Sm had the highest emission intensity. [31]

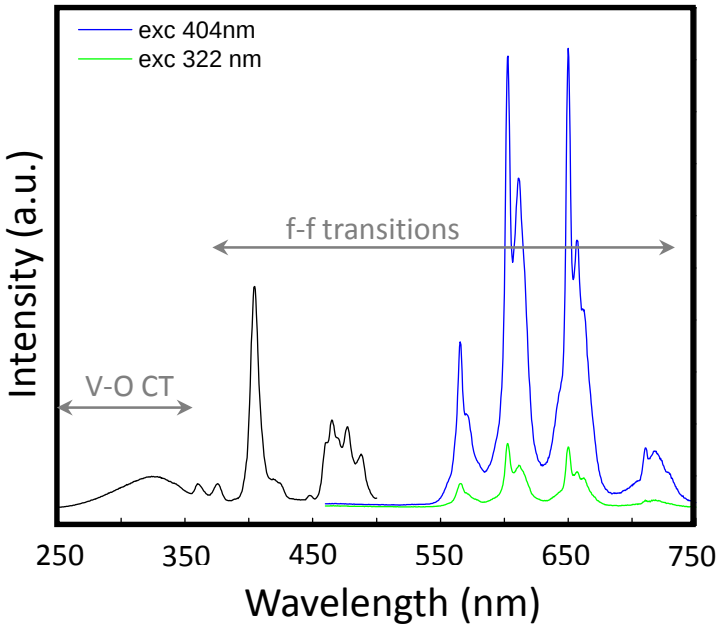

Figure 9: Room-temperature combined excitation-emission spectra of 2%Sm:$La_7O_6(VO_4)_3$.

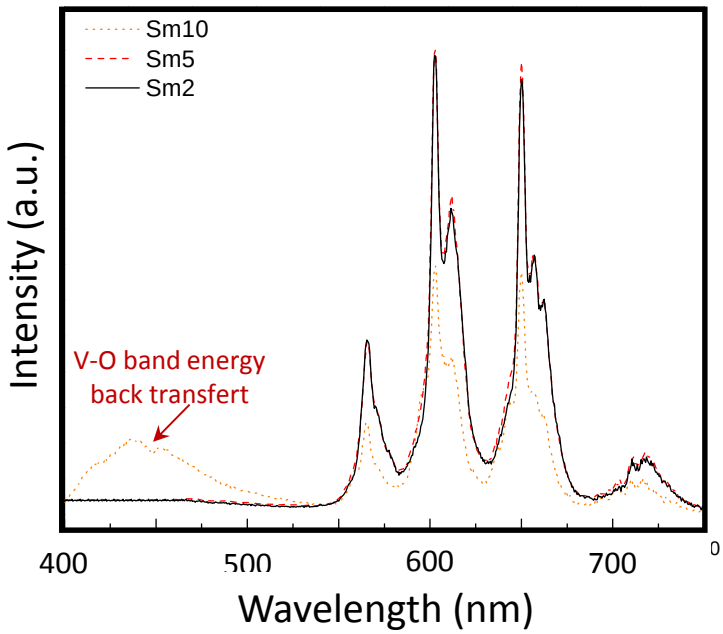

Figure 10: Emission spectra of 2%Sm:$La_7O_6(VO_4)_3$, 5%Sm:$La_7O_6(VO_4)_3$, and 10%Sm:$La_7O_6(VO_4)_3$ (excited at 464 nm).

Finally, the luminescence decay times were measured for the Sm^{3+} compositions. The decay profiles for the 2%. 5% and 10% samples are shown in SI (Figures S13-S15). In these cases, the data were recorded only for the most intense emission, *i.e.* when exciting into the 404 nm f-f transition. In order to obtain a good fit, a biexponential function had to be used. A table that summarizes the decay times for the 2%, 5% and 10% samples is given in Table 4. We observe an increase in the decay time at higher Sm^{3+} concentrations. The highest decay time was recorded for the 10% Sm sample (t1 = 3.6 μs, t2 = 21.3 μs). This can be caused by migration processes between the ions, which are increased at higher Sm^{3+} concentrations. The QYs of the samples were in all cases below 1%.

Table 4: Luminescence decay times of Sm:$La_7O_6(VO_4)_3$ samples

Sample (exc at 404 nm)	τ1 (μs)	τ2 (μs)
2%Sm:$La_7O_6(VO_4)_3$	2.8	16.6
5%Sm:$La_7O_6(VO_4)_3$	2.9	17.5
10%Sm:$La_7O_6(VO_4)_3$	3.6	21.3

Conclusion

In this paper, two polytypes of the new oxyvanadate matrix $La_7O_6(VO_4)_3$ were solved and refined combining precession electron and X-Ray diffraction data. The low temperature α-polytype is a NCS material based on OLa_4 oxo-centered units building a 3D porous framework hosting vanadate groups. The high temperature β-polytype is CS with a similar backbone. This matrix was tested as a potential phosphor by substitution of La^{3+} by Eu^{3+} and Sm^{3+} at three different ratios (2%, 5% and 10%). Under the excitation wavelength at 464nm for Eu^{3+} and 404 for Sm^{3+} (in the f-f band), the doped materials emit in the orange-red visible light with highest emitting between 578-706nm ($^5D_0 \rightarrow {}^7F_{0\text{-}4}$) for Eu^{3+} and between 560-709nm ($^5G_{5/2} \rightarrow {}^6H_{5/2\text{-}11/2}$) for Sm^{3+}. The lanthanides could also be excited into the V-O charge transfer in the UV, but this excitation was less efficient. For Sm^{3+}, the strongest emitting intensity was observed at 5% doping rate and for Eu^{3+} at 10%. The decay time was also studied and fitted with a biexponential function. The QY were

measured below 1% for Sm^{3+} doped samples and up to around 2.5% for Eu^{3+} doped ones. Although these values are low there is clearly visible a rise in the QYs values upon concentration increase.

ASSOCIATED CONTENT

Supporting Information

The Supporting Information is available free of charge on the ACS Publications website xxxx at DOI: xxxx.

Crystal structure details, Rietveld refinements, SEM images, TR-SHG data, XRF analysis and luminescence study (RT excitation-emission spectra, decay profiles.

AUTHOR INFORMATION

Corresponding Author

* E-mail: Marie.Colmont@centralelille.fr

Author Contributions

The manuscript was written through contributions by all authors.

Notes

The authors declare no competing financial interests.

Acknowledgments

M.C. thank L. Burylo and N. Djellal for their technical assistance. The Chevreul Institute (FR 2638), the Ministère de l'Enseignement Supérieur et de la Recherche, the Région Hauts-de-France , the CNRS, and the FEDER are acknowledged for supporting and funding XRD and TEM facilities.

A.M.K. thanks Prof. Rik Van Deun for access to the Edinburgh Instruments FLSP920 setup.

REFERENCES

[1] K. A. Gschneidner, J.-C. G. Bünzli, and V. K. Pecharsky, *Optical spectroscopy*. Amsterdam; Boston: Elsevier North-Holland, **2007**.

[2] K. A. Gschneidner, J.-C. G. Bünzli, and V. K. Pecharsky, « Preface », in *Handbook on the Physics and Chemistry of Rare Earths*, **2011**, *41*, Elsevier, p. v‑ x.

[3] A. M. Kaczmarek and R. Van Deun, « Rare earth tungstate and molybdate compounds – from 0D to 3D architectures », *Chem. Soc. Rev.*, **2013**, *42*(23), 8835.

[4] G. Blasse and B. C. Grabmaier, *Luminescent Materials*. Berlin, Heidelberg: Springer Berlin Heidelberg, **1994**.

[5] W. M. Yen, S. Shionoya, and H. Yamamoto, Éd., *Phosphor handbook*, 2. ed. Boca Raton, Fla.: CRC Press, **2007**.

[6] A. M. Kaczmarek, K. Van Hecke, and R. Van Deun, « Nano- and micro-sized rare-earth carbonates and their use as precursors and sacrificial templates for the synthesis of new innovative materials », *Chem. Soc. Rev.*, **2015**, *44*(8), 2032‑ 2059.

[7] J.-C. G. Bünzli and C. Piguet, « Taking advantage of luminescent lanthanide ions », *Chem. Soc. Rev.*, **2005**, *34*(12), 1048.

[8] E. Cavalli, F. Angiuli, A. Belletti, and P. Boutinaud, « Luminescence spectroscopy of YVO4:Ln^{3+}, Bi^{3+} (Ln^{3+}=Eu^{3+}, Sm^{3+}, Dy^{3+}) phosphors », *Opt. Mater.*, **2014**, *36*(10), 1642‑ 1648.

[9] V. Singh, S. Takami, N. Aoki, D. Hojo, T. Arita, and T. Adschiri, « Hydrothermal synthesis of luminescent $GdVO_4$:Eu nanoparticles with dispersibility in organic solvents », *J. Nanoparticle Res.*, **2014**, *16*(5), 2378.

[10] K. N. Shinde, S. Roshani, and S. J. Dhoble, « Photoluminescence characteristics of the single-hostwhite-light-emitting $Sr_{3-3x/2}(VO_4)_2$:xEu (0<x<0.3)phosphors for LEDs », *Journal of Luminescence*, **2014**, 91‑ 96.

[11] C. Qin, Y. Huang, and H. J. Seo, « Structure and Luminescence of New Red-Emitting Materials-Eu $^{3+}$ -Doped Triple Orthovanadates Na*A*La$(VO_4)_2$ (*A* = Ca,Sr,Ba) », *J. Am. Ceram. Soc.*, **2013**, *96*(4), 1181‑ 1187.

[12] X. Zhou, L. Chen, S. Jiang, G. Xiang and L. Li , « Eu^{3+}activated $LiSrVO_4$ phosphors: Emission color tuning and potentialapplication in temperature sensing », *Dyes and Pigments*, **2018**, 219‑ 226.

[13] Z. Tao, T. Tsuboi, Y. Huang, W. Huang, P. Cai, et H. J. Seo, « Photoluminescence Properties of Eu $^{3+}$ -Doped Glaserite-Type Orthovanadates $CsK_2Gd[VO_4]_2$ », *Inorg. Chem.*, **2014**, *53*(8), 4161‑ 4168.

[14] M. Colmont, S. Saitzek, A. Katelnikovas, H. Kabbour, J. Olchowka, et P. Roussel, « Host-sensitized luminescence properties of $KLa_5O_5(VO_4)_2$:Eu^{3+} for solid-state lighting applications », *J. Mater. Chem. C*, **2016**, *4*(30), 7277‑ 7285.

[15] L. Palatinus, « PETS a Computer Program for Analysis of Electron Diffraction Data ». **2011**.

[16] L. Palatinus, M. Klementová, V. Dřínek, M. Jarošová, and V. Petříček, « An Incommensurately Modulated Structure of η′-Phase of $Cu_{3+x}Si$ Determined by Quantitative Electron Diffraction Tomography », *Inorg. Chem.*, **2011**, *50*(8), 3743‑ 3751.

[17] L. Palatinus and G. Chapuis, « SUPERFLIP – a computer program for the solution of crystal structures by charge flipping in arbitrary dimensions », *J. Appl. Crystallogr.*, **2007**, *40*(4), 786‑ 790.

[18] V. Petříček, M. Dušek, and L. Palatinus, « Crystallographic Computing System JANA2006: General features », *Z. Für Krist. - Cryst. Mater.*, **2014**, *229*(5).

[19] L. Yuan, S. Clevers, N. Couvrat, Y. Cartigny, V. Dupray, and G. Coquerel, « Precise Urea/Water Eutectic Composition by Temperature-Resolved Second Harmonic Generation », *Chem. Eng. Technol.*, **2016**, *39*(7), 1326‑ 1332.

[20] L. Yuan, S. Clevers, A. Burel, P. Negrier, M. del Barrio, B. Ben Hassine, D. Mondieig, V. Dupray, J. Li and G. Coquerel « New Intermediate Polymorph of 1-Fluoro-adamantane and Its Second-Order-like Transition toward the Low Temperature Phase », *Cryst. Growth Des.*, **2017**, *17*(6), 3395‑ 3401.

[21] M. Colmont, L. Palatinus, M. Huvé, H. Kabbour, S. Saitzek, N. Djelal and P. Roussel , « On the Use of Dynamical Diffraction Theory To Refine Crystal Structure from Electron Diffraction Data: Application to $KLa_5O_5(VO_4)_2$, a Material with Promising Luminescent Properties », *Inorg. Chem.*, **2016**, *55*(5), 2252‑ 2260.
[22] A. Boultif and D. Louër, « Powder pattern indexing with the dichotomy method », *J. Appl. Crystallogr.*, **2004**, *37*(5), 724‑ 731.
[23] U. Kolb, T. Gorelik, C. Kübel, M. T. Otten, and D. Hubert, « Towards automated diffraction tomography: Part I—Data acquisition », *Ultramicroscopy*, **2007**, *107*(6‑ 7), 507‑ 513.
[24] B. Ewald, Yu. Prots, and R. Kniep, « Refinement of the crystal structures of praseodymium- and samariumoxoborate- bis(oxophosphate)-oxide, $Ln_7O_6[BO_3][PO_4]_2$, (Ln = Pr, Sm) », *Z. Für Krist. - New Cryst. Struct.*, **2004**, *219*(1‑ 4).
[25] I. Radosavljevic, J. S. O. Evans, and A. W. Sleight, « Synthesis and Structure of BiCa2VO6 », *J. Solid State Chem.*, **1998**, *137*(1), 143‑ 147.
[26] I. Radosavljevic, J. A. K. Howard, and A. W. Sleight, « Synthesis and structure of two new bismuth cadmium vanadates, $BiCdVO_5$ and $BiCd_2VO_6$, and structures of $BiCa_2AsO_6$ and $BiMg_2PO_6$ », *Int. J. Inorg. Mater.*, **2000**, *2*(6), 543‑ 550.
[27] O. Labidi, P. Roussel, M. Drache, R.-N. Vannier, and J.-P. Wignacourt, « Polymorphism in $PbBiOXO_4$ compounds (X=V, P, As): Part II—$PbBiOPO_4$ and $PbBiOAsO_4$ structures and characterization of related solid solutions », *J. Solid State Chem.*, **2008**,. *181*(9), 2268‑ 2273.
[28] P. Roussel, O. Labidi, M. Huve, M. Drache, J.-P. Wignacourt, et V. Petricek, « The incommensurately modulated crystal structure of β-Pb_2BiVO_6 : interpretation of the phase transition $\alpha \rightarrow \beta \rightarrow \delta$ and conduction properties of related materials », *Acta Crystallogr. B*, **2009**, *65*(4), 416‑ 425.
[29] R. D. Shannon, « Revised effective ionic radii and systematic studies of interatomic distances in halides and chalcogenides », *Acta Crystallogr. Sect. A*, **1976**, *32*(5), 751‑ 767.
[30] A. M. Kaczmarek, K. Van Hecke, et R. Van Deun, « Enhanced Luminescence in Ln^{3+} -Doped Y_2WO_6 (Sm, Eu, Dy) 3D Microstructures through Gd^{3+} Codoping », *Inorg. Chem.*, **2014**, *53*(18), 9498‑ 9508.
[31] M. Sobczyk, D. Szymański, M. Guzik, et J. Legendziewicz, « Optical behaviour of samarium doped potassium yttrium double phosphates », *J. Lumin.*, **2014**, *169*, 794‑ 798.
[32] B. Yan, « Rare Earth, Rare Earth Luminescence, Luminescent Rare Earth Compounds, and Photofunctional Rare Earth Hybrid Materials », in *Photofunctional Rare Earth Hybrid Materials*, **2017**, *251*, Singapore: Springer Singapore, 3‑ 21.
[31] Z. Jing, Y. Meihua, C. Yi, Z. Zhuohui, G. Xinchen, X. Jiyun, Z. Yang, X. Kai, Y. Hongwei, "Structure–Optical Behavior Correlation, Optimized Photoluminescence, and DFT Calculation of $La_7O_6(BO_3)(PO_4)_2:Sm^{3+}$ Micropowder for Solid State Lighting", *ACS Appl. Electron. Mat.*, **2019**, 1(8), 1688-1697

Table of Content

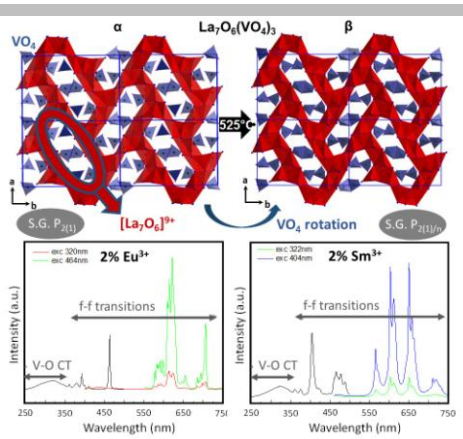

María Alejandra Gómez Torres, Gilles H. Gauthier, Anna M. Kaczmarek, Marielle Huvé, Pascal Roussel, Valérie Dupray, Lina Yuan, Anastasiya Zadoya, Marie Colmont*

Pure and RE^{3+}-doped $La_7O_6(VO_4)_3$ (RE= Eu,Sm) : polymorphism stability and luminescence properties of a new oxyvanadate matrix.

The new $La_7O_6(VO_4)_3$ was evidenced as two polymorphs α and β. The structure was solved using both electron diffraction and Rietveld refinement. The luminescence properties were studied after doping by 2%, 5% and 10% of Sm^{3+} and Eu^{3+}.